The Astrophysical Journal, 753:139 (16pp), 2012 July 10 doi:10.1088/0004-637X/753/2/139

A MULTI-EPOCH TIMING AND SPECTRAL STUDY OF THE ULTRALUMINOUS X-RAY NGC 5408 X-1 WITH *XMM-Newton*

Pasham R. Dheeraj[1] and Tod E. Strohmayer[2]
[1] Astronomy Department, University of Maryland, College Park, MD 20742, USA; dheeraj@astro.umd.edu
[2] Astrophysics Science Division, NASA's Goddard Space Flight Center, Greenbelt, MD 20771, USA; tod.strohmayer@nasa.gov
Received 2012 January 27; accepted 2012 May 6; published 2012 June 22

ABSTRACT

We present results of new *XMM-Newton* observations of the ultraluminous X-ray source (ULX) NGC 5408 X-1, one of the few ULXs to show quasi-periodic oscillations (QPOs). We detect QPOs in each of four new (≈100 ks) pointings, expanding the range of frequencies observed from 10 to 40 mHz. We compare our results with the timing and spectral correlations seen in stellar-mass black hole systems, and find that the qualitative nature of the timing and spectral behavior of NGC 5408 X-1 is similar to systems in the steep power-law state exhibiting Type-C QPOs. However, in order for this analogy to quantitatively hold we must only be seeing the so-called *saturated* portion of the QPO frequency—photon index (or disk flux) relation. Assuming this to be the case, we place a lower limit on the mass of NGC 5408 X-1 of $\gtrsim 800\,M_{\odot}$. Alternatively, the QPO frequency is largely independent of the spectral parameters, in which case a close analogy with the Type-C QPOs in stellar systems is problematic. Measurement of the source's timing properties over a wider range of energy spectral index is needed to definitively resolve this ambiguity. We searched all the available data for both a broad Fe emission line as well as high-frequency QPO analogs (0.1–1 Hz), but detected neither. We place upper limits on the equivalent width of any Fe emission feature in the 6–7 keV band and of the amplitude (rms) of a high-frequency QPO analog of ≈10 eV and ≈4%, respectively.

Key words: accretion, accretion disks – methods: observational – X-rays: binaries

Online-only material: color figures

1. INTRODUCTION AND BACKGROUND

Ultraluminous X-ray sources (ULXs) are bright, point-like, off-nuclear extragalactic X-ray sources. Since their discovery over two decades ago (Fabbiano 1989), the true nature of these sources has been a mystery. Their isotropic X-ray luminosities range from a few $\times 10^{39}$ erg s^{-1} to as high as 10^{42} erg s^{-1}. Luminosities at the high end of this range are found in a handful of sources which have been dubbed hyperluminous X-ray sources (HLXs, e.g., M82 X-1: Matsumoto et al. 2001; Kaaret et al. 2001; HLX ESO 243-49 X-1: Miniutti et al. 2006; Farrell et al. 2009). The apparent X-ray luminosities of these sources exceed the Eddington limit for any known stellar-mass black hole (StBH), hence the term "ultraluminous."

Based on their variability on short timescales (some ULXs are known to vary on timescales of the order of a few minutes) and high luminosities, some ULXs are almost certainly powered by accretion onto black holes (excluding the population of X-ray bright supernovae; Immler & Lewin 2003). The controversy, however, is with their mass range. Black holes, in principle, can exist in three mass ranges. StBHs (Mass ~ 3–50 $M_{\odot}$) are the remnants of stellar evolution of massive normal stars (stars excluding the Population III category). On the opposite end of the mass scale are the supermassive black holes (SMBHs: Mass ~ 10^6 to $10^{10} M_{\odot}$), which are currently theorized to form either via accretion onto "seed" black holes in the early universe (~few Myrs after the big bang) with subsequent mergers (Volonteri et al. 2003; Davies et al. 2011) or via direct collapse of dense gas (Begelman et al. 2006). Their exact formation scenario is still somewhat uncertain. Finally, one has the intermediate-mass black holes (IMBHs; mass range 100 to few × 1000 $M_{\odot}$), whose formation mechanisms are the subject of considerable debate. There are a number of processes whereby an IMBH can form. For example, they can be formed at the centers of globular clusters via accretion onto a massive black hole (Mass ~ 50 $M_{\odot}$) over a time period of 10^{10} yr (Miller & Hamilton 2002), by accretion onto a primordial black hole (e.g., Mack et al. 2007), or by mergers of seed black holes.

The off-centered nature of ULXs rules them out as candidates for SMBHs. Given the ages of their host galaxies, if they were SMBHs, they should have sunk to the centers of their galaxies due to dynamical friction (Miller & Colbert 2004). Clearly, this is not the case. This leaves the possibility of their being either StBHs or IMBHs. Theories supporting the idea of an StBH as the central engine often employ either beamed X-ray emission or some sort of super-Eddington emission mechanism to explain the observed high luminosities. Current ideas include geometric beaming (King et al. 2001), relativistic beaming similar to the phenomenon of blazars (Körding et al. 2002), and super-Eddington emission as a result of a photon-bubble instability in radiation-dominated accretion disks (Begelman 2002). More recently, based on high-quality *XMM-Newton* spectra of 12 ULXs, Gladstone et al. (2009) have suggested that ULXs might be accreting StBH systems in a new *ultraluminous accretion state* (an addition to the current classification of black hole accretion states: thermal (high/soft), hard (low/hard), and steep power law (SPL; very high) as in McClintock & Remillard 2006), where accretion is again super-Eddington. Alternatively, it has been suggested that these sources might be powered by gravitational energy release from accretion onto an IMBH (Colbert & Mushotzky 1999). This presents a relatively simpler solution, where the energetics proceed similarly to that of the StBH systems (at sub-Eddington accretion rates) with the corresponding physical properties scaling appropriately with the mass of the compact object. It is also possible that ULXs constitute an inhomogeneous population of both StBHs and IMBHs.

It is now known that certain characteristic timescales in accreting black hole systems scale with the mass of the black hole. For example, McHardy et al. (2006) have established that

in soft-state StBHs and active galactic nuclei (AGNs), the break timescale of the power density spectrum (PDS), the mass of the black hole, and the luminosity are strongly correlated. Their work was further extended to the hard-state StBHs by Körding et al. (2007). These studies strongly demonstrate that certain physical timescales of accreting compact objects scale directly with the mass of the source (after accounting for differences in accretion rates, i.e., luminosity). Therefore, timing studies can play a key role in extracting valuable information about the mass of the compact source, which is crucial in the case of ULXs in order to better understand the nature of the emission processes that result in such high apparent luminosities. Of particular interest here are the low-frequency quasi-periodic oscillations (LFQPOs). Within the context of StBHs, the LFQPOs (those in the range ~0.1–15 Hz) are broadly classified into three categories based on their properties and the overall nature of their PDS (Casella et al. 2005). The PDS with type-A and -B quasi-periodic oscillations (QPOs) is characterized by weak red noise (noise at the low-frequency end of the PDS) with the type-A QPOs occurring with relatively low coherence (quality factor, Q: centroid frequency/FWHM $\lesssim 3$) compared to the type-B ($Q \gtrsim 6$). Finally, one has the type-C QPOs which are most relevant to the present work. The PDS accompanying these QPOs in StBH systems can be described by a flat-topped, band-limited noise breaking to a power law with the QPOs evident on the power-law portion of the spectrum, close to the break.

Further, the type-C QPOs are fairly coherent with the quality factor, Q from 5 to 15 and amplitudes (% rms) ranging from 2 to 20. In StBHs, they are known to occur in the frequency range from ≈0.1 to 15 Hz. In light of the work unifying the StBHs and the SMBHs, if some ULXs were to host IMBHs, then the qualitative behavior of their PDS should be comparable to StBHs with the characteristic variability times scaling according to the mass of the putative IMBH. This idea has been explored by a number of authors to search for the "QPO analogs" in ULXs; and QPOs have now been detected in a handful of them. The QPOs detected in M82 X-1 (Strohmayer & Mushotzky 2003), NGC 5408 X-1 (Strohmayer et al. 2007), and NGC 6946 X-1 (Rao et al. 2010) resemble the type-C QPOs, while those detected in the M82 source X42.3+59 more closely resemble the type-A or -B QPOs (Feng et al. 2010). The crucial difference here is that the QPO centroid frequencies of the ULX sources appear to be scaled down by a factor of a few ×(10–100) (~few mHz) compared to the LFQPOs in StBHs.

Under the assumption that the ULX mHz QPOs are analogs of the LFQPOs in StBHs, it is reasonable to assume that their characteristic timescales/frequencies (e.g., QPO centroid frequencies, PDS break frequencies) scale with the mass of the accreting source and vice versa. However, the type-C QPOs occur with a wide range of centroid frequencies (0.1–15 Hz) in StBH systems. Therefore, timing information alone is not sufficient to accurately estimate ULX masses in this way, but combining timing and spectral information has proven to be a valuable tool. For example, in StBH systems, the power-law photon index and disk flux are correlated with the QPO centroid frequency. The general trend is an increase in power-law photon index and disk flux with the QPO centroid frequency (e.g., Sobczak et al. 2000; Vignarca et al. 2003; Shaposhnikov & Titarchuk 2009), with evidence for saturation (constancy of the power-law photon index and disk flux with a further increase in QPO centroid frequency) beyond a certain frequency.

Using a reference StBH system with a measured QPO centroid-frequency–photon-index relation, one can then scale the QPO centroid frequencies detected in ULX systems at a given power-law spectral index to get an estimate of the mass. For example, with archival *XMM-Newton* data from M82 X-1, Dewangan et al. (2006) extracted the energy and power spectra of the source. The PDS was strikingly reminiscent of an StBH with type-C QPOs, i.e., flat-top noise breaking to a power law with QPOs on the power-law portion of the spectrum. However, the respective timescales were scaled down by a factor of ~10. The QPO in this case was centered around a frequency of ~114 mHz and the energy spectrum had a power-law photon index of ~2.0. Using the QPO-frequency–photon-index correlations from two StBH reference sources, GRS 1915+105 and XTE J1550−564, they estimated the mass of the ULX in M82 X-1 by scaling its QPO centroid frequency (~114 mHz) at the given photon index (~2.0). They estimated the mass of the black hole to be in the range 25–520 $M_\odot$. Similar scaling arguments were used by Rao et al. (2010) to estimate the mass of the black hole in the ULX NGC 6946 X-1 to be in the range (1–4) × 1000 $M_\odot$. Based on both the PDS and the energy spectrum of NGC 5408 X-1, Strohmayer & Mushotzky (2009, hereafter S09) argued that the source behavior was consistent with the SPL state often seen in StBHs. They compared the available data from NGC 5408 X-1 to five different StBH reference sources and estimated the mass of the black hole to be a few ×1000 $M_\odot$. Feng et al. (2010) detected 3–4 mHz QPOs from the ULX X42.3+59 in M82 and identified them as either type A/B analogs of StBHs. They estimated the mass of the black hole to be in the range 12,000–43,000 $M_\odot$ by scaling the QPO frequency to that of the type A/B QPOs in StBHs.

It is important to note that the above scaling arguments have several caveats. First, the mass estimates were established under the assumption that the mHz QPOs detected from these ULX systems are analogous to a particular type of LFQPO detected in StBH systems, i.e., A, B, or C. These identifications were based on the qualitative nature of the power spectrum (PDS) alone in some cases and both the PDS and the energy spectrum in the case of NGC 5408 X-1. Second, in the case of the ULX mHz QPOs, the observed range of QPO centroid frequencies and photon indices has been limited. To gain a more secure identification one would like to see the QPO frequencies and photon spectral indices correlate in a similar fashion as for the StBHs.

In this paper, we further explore these issues using extensive new observations of NGC 5408 X-1 with *XMM-Newton*. We describe the properties of the mHz QPOs over a wider range of centroid frequencies than previous data allowed. More specifically, we study the nature of the mHz QPOs from NGC 5408 X-1 through a systematic search for timing–spectral correlations similar to those seen in the StBHs. The paper is arranged as follows. In Section 2, we describe the data used for the present study. In Section 3, we show the results from our timing analysis, while in Section 4 we give details of the energy spectral analysis. In Section 5, we describe our search for timing–spectral correlations similar to those seen in accreting StBH systems. The search is conducted using two different spectral models, a phenomenological model of a *multi-colored disk + power-law* and then with a model describing Comptonization by bulk motion (Titarchuk et al. 1997) that has been used previously to derive black hole masses from QPO scaling arguments (Shaposhnikov & Titarchuk 2009). Finally, in Section 6 we discuss the implications of our results on the mass of the black hole in NGC 5408 X-1.

Table 1
Summary of the *XMM-Newton* Observations of NGC 5408 X-1

ObsID	T_{obs}[a] (ks)	Net Count Rate[b] (counts s^{-1})	Effective Exposure[c] (ks)
0302900101 (2006)	132.25	1.26 ± 0.04	99.94
0500750101 (2008)	115.69	1.19 ± 0.04	48.55
0653380201 (2010A)	128.91	1.46 ± 0.04	80.68
0653380301 (2010B)	130.88	1.40 ± 0.04	110.0
0653380401 (2011A)	121.02	1.34 ± 0.07	107.75
0653380501 (2011B)	126.37	1.31 ± 0.07	98.66

Notes.
[a] The total observation time.
[b] The average *pn+MOS* count rate.
[c] After accounting for flaring background and good time intervals. See Sections 2 and 3 for details on filtering.

2. *XMM-Newton* OBSERVATIONS

XMM-Newton has now observed NGC 5408 X-1 on multiple occasions. We use data from six of the most recent observations (~100 ks each) spread over a time span of five years (2006–2011). The details of the observations are outlined in Table 1. Results from the first two observations (in 2006 and 2008, respectively) were summarized in Strohmayer et al. (2007, hereafter S07, S09). Using the 2006 data, S07 reported the first detection of quasi-periodic variability from this source. S09's analysis of the 2008 observation again showed evidence for the presence of QPOs. However, the most prominent QPO during the 2008 observation was at a lower frequency (QPO at ~10 mHz compared to 20 mHz in 2006). Further, S09 noted that the disk contribution to the total flux and the power-law index of the energy spectrum decreased slightly compared to its state in 2006. This is analogous to a trend often seen in StBH systems where the disk flux and the power-law index of the energy spectrum positively correlate with the centroid frequency of the most dominant QPOs (e.g., Vignarca et al. 2003; Sobczak et al. 2000). These findings were used to propose additional observations with *XMM-Newton*, with the goal of detecting QPOs over a range of frequencies and hence to further explore for correlations between timing and energy spectral properties. A large program was approved for Cycle 9 (PI: Strohmayer), and four observations (~100 ks each) were made under this program. Two of the observations were carried out in 2010 (2010a and 2010b) and the rest in 2011 (2011a and 2011b). Here, we present results from these new observations as well as a reanalysis of the earlier pointings, so as to facilitate a consistent comparison of all the available data.

For the present work, we use the data acquired by the European photon imaging camera (EPIC), i.e., both the *pn* and *MOS* to get a higher signal-to-noise ratio (S/N) in the power and energy spectra. We used the standard SAS version 11.0.0 to reduce the images and filtered event lists from all the EPIC data. The standard filter with *(PATTERN ⩽ 4)*, to include only single and double pixel events, was applied to the event lists and events only in the energy range 0.3–12.0 keV were considered for further analysis. Background flaring was prominent for brief periods during certain observations. The power and energy spectra were carefully extracted taking into account both the background flaring and the instrumental dead time effects (specific details in the next sections). In all the observations, the source was easily detectable and we did not face any source confusion problems. We extracted source events from a region of radius 32″ centered around the source. This particular value was chosen to roughly include 90% of the light from the source (estimated from the fractional encircled energy of the EPIC instruments). A background region, free of other sources, was extracted in a nearby region. The size of the background region was chosen to be consistent with the source region. Further, the size of the source and the background region was chosen to be consistent for all the six observations (i.e., 32″). We present the specific details of the timing and spectral analysis in the following sections.

3. TIMING ANALYSIS

We first produced the source and the background light curves to assess the quality of the data. Shown in the left panels of Figures 1(A) and (B) are the background count rates (*pn+MOS1+MOS2*) for each of the six observations. Overlaid are the time intervals during which a given instrument (*pn, MOS1/2*) was continuously active for more than 5 ks, i.e., all the instrumental good time intervals (GTIs) longer than 5 ks. For a given instrument, a horizontal line (offset to an arbitrary value for each instrument) indicates the active time, while a vertical line marks the beginning or the end of a continuous data interval. Such an insight is important as we are using both the *pn* and the *MOS* data to achieve higher count rates compared to, say, the *pn* alone. In other words, this ensures that the combined *pn* and *MOS* event lists contain only events corresponding to the times during which all the three instruments were active. Furthermore, inspection of the light curves reveals background flaring at either the beginning or the end, or both, of all the observations. Therefore, the final combined *(pn+MOS1+MOS2)* light curves were extracted by taking into account the GTIs of all the instruments and excluding the periods of background flaring. The filtered light curves (100s bins) of the source and the non-flaring background in the energy range 0.3–12.0 keV are shown in the right panels of Figures 1(A) and (B). The combined mean count rates (0.3–12.0 keV) during each observation are listed in Table 1. Note that the gaps in the data are either due to exclusion of background flaring times, dead time intervals, or the absence of GTIs longer than 5 ks.

It is evident from the light curves (right panels of Figures 1(A) and (B)) that the source varies significantly during all the observations. To quantify the variability, we construct a PDS from each of the light curves. To achieve higher S/N in the PDS, we break the GTIs into shorter segments (S/N $\propto \sqrt{}$Number of individual spectra; e.g., Van der klis 1989) and derive an average power spectrum. For a given observation, the size and the number of such segments are shown in the first row of Table 2. Figures 2(A) and (B) show the PDS and the best-fitting model (thick solid line) for each of the six observations in two different energy bands. Shown in the left panel is a PDS in an energy band in which a QPO is detected with high statistical significance and in the right panel is a PDS derived from photons in the energy band of 1.0–10.0 keV (the reason for constructing power spectra in two different energy bands is discussed in the next paragraph). All the power spectra shown here use the so-called Leahy normalization, with the Poisson noise level being 2 (Leahy et al. 1983). Clearly, in each spectrum the power rises below ~0.1 Hz with evidence for a QPO in the range of 10–40 mHz and essentially Poisson noise at higher frequencies.

To quantify this behavior, we fit a bending power law to the continuum and a Lorentzian to model the QPO (Belloni et al. 2002). The model fits well with the reduced $\chi^2 \approx 1$ (last row of Tables 2 and 3) in three cases (2008, 2011A, 2011B) and gives acceptable fits with the reduced χ^2 in the

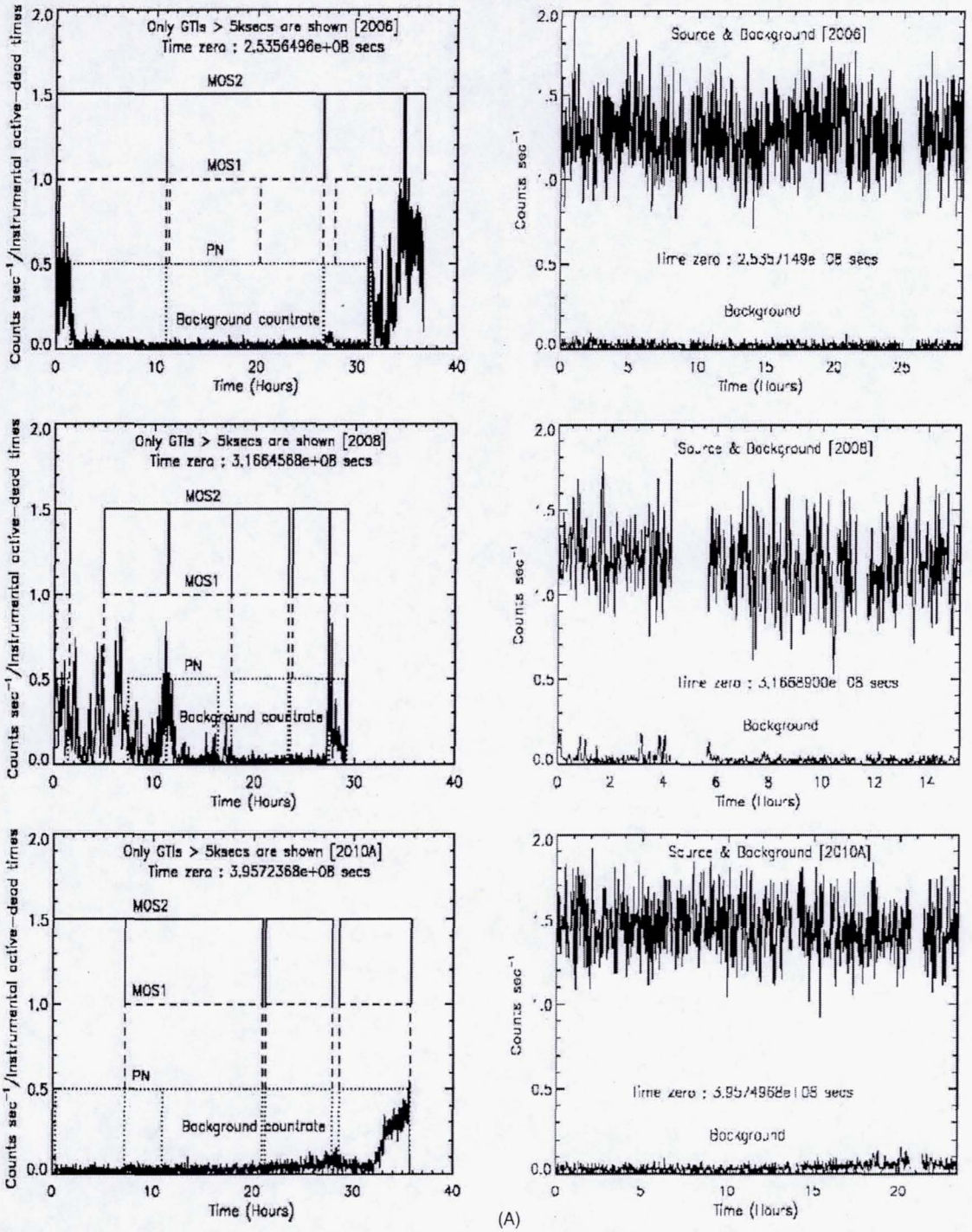

Figure 1. Left panel: good time intervals (>5 ks) from EPIC-pn, MOS1, and MOS2 on board *XMM-Newton*. For a given instrument, at a given time (*X*-axis), a finite value on the *Y*-axis implies the instrument was *continuously* active for at least 5 ks. Also shown is a combined background (pn+MOS1+MOS2) light curve with flaring evident in some cases. The observation year is indicated at the top of each plot ((A) 2006, 2008, and 2010A data; (B) 2010B, 2011A & 2011B data: see Table 1). Time zero is indicated in seconds since 1998.0 TT. Right panel: filtered light curves (pn+MOS1+MOS2) accounting for both instrumental dead times and flaring. The power spectra were derived from these cleaned light curves. These light curves were extracted using photons in the energy range of 0.3–10.0 keV.

range 1.3–1.5 (last row of Tables 2 and 3) in the other three cases (2006, 2010A, 2010B). A careful analysis of the residuals in the latter three cases indicates that multiple weak features contribute significantly to increase the overall χ^2. For example, in the case of the PDS derived from the 2010A data (bottom two panels of Figure 2(A)), the weak QPO-like feature at ~55 mHz and the excess at ~0.2 Hz contribute about 30 to the total χ^2. However, their individual statistical significance is rather low. Nevertheless, for the purposes of analyzing the QPO properties and studying the overall qualitative nature of the power spectra, the fits are adequate. The best-fitting model parameters (derived from a fit in the frequency range 1.0 mHz–0.5 Hz) for each observation are shown in Tables 2 and 3 for the two different energy bands (highlighted in the tables). Also shown are the

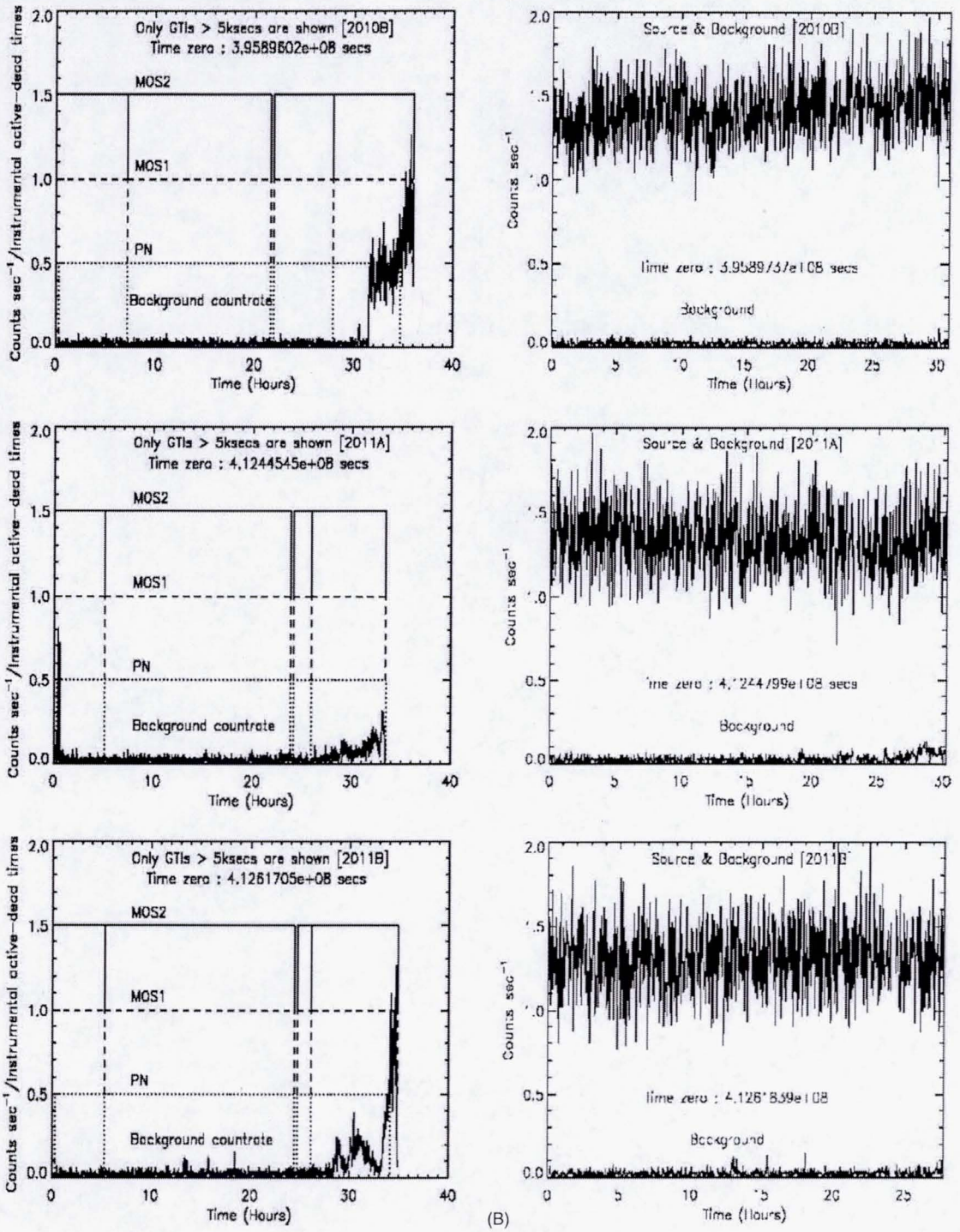

(B)

Figure 1. (Continued)

χ^2/degrees of freedom (dof) values for each of the fits along with the χ^2/dof corresponding to the continuum model (in braces). The change in χ^2 serves as an indicator of the statistical significance of the QPOs. For a given observation, we choose two different energy bands: the first energy band (second row of Table 2) is the bandpass in which the QPO is detected with a very high confidence and the second bandpass of 1.0–10.0 keV was chosen to consistently compare the properties of the QPO across all the observations (overall variability is energy dependent). We confirm the overall qualitative nature of the PDS, that is, flat-topped noise breaking to a power law with a QPO on the power-law portion (near the break). This is consistent with StBHs showing type-C QPOs but with the characteristic frequencies scaled down by a factor of a few $\times 10$. This is in agreement with the results reported by S07 and S09, except with regard to possible close QPO pairs, as here all our PDSs (Figures 2(A) and (B)) are averaged to the extent of smearing out weak features (to clearly identify the strongest QPO). The effect of averaging

Table 2
Summary of the Best-fitting Model Parameters for the Power Density Spectra (PDS) of the ULX NGC 5408 X-1

Data Set	2006	2008	2010A	2010B	2011A	2011B
Exposure [a](ks)	27.6 × 3	15.5 × 2	23.2 × 3	21.0 × 4	67.4 × 1	55.0 × 1
Energy Range[b] (keV)	0.30–2.0	1.0–10.0	0.85–10.0	1.0–4.0	1.10–8.0	1.20–2.0
Count rate[c] (counts s^{-1})	1.17 ± 0.03	0.43 ± 0.02	0.71 ± 0.02	0.50 ± 0.01	0.41 ± 0.02	0.23 ± 0.01
C[d]	1.95 ± 0.01	1.81 ± 0.02	1.95 ± 0.02	2.00 ± 0.01	1.95 ± 0.02	1.92 ± 0.02
A[d]	0.86 ± 1.05	3.39 ± 2.90	9.14 ± 17.90	$(0.80 \pm 2.30) \times 10^{-04}$	3.49 ± 10.61	$(2.11 \pm 3.47) \times 10^{-03}$
$\Gamma_{\rm Low}$[d]	0.20 ± 0.19	0.09 ± 0.13	-0.25 ± 0.31	2.68 ± 0.98	-0.04 ± 0.42	1.45 ± 0.52
$\nu_{\rm bend}$[d] (mHz)	6.33 ± 0.75	6.34 ± 0.49	10.26 ± 6.03	30.63 ± 20.20	5.80 ± 4.84	7.15 ± 8.67
$\Gamma_{\rm High}$[d]	6.74 ± 3.34	10.25 ± 5.60	1.60 ± 0.50	0.25 ± 0.17	1.98 ± 1.83	-0.09 ± 0.43
$N_{\rm QPO,1}$[e]	1.88 ± 0.16	3.51 ± 1.69	0.63 ± 0.15	0.72 ± 0.21	2.10 ± 0.56	1.04 ± 0.29
$\nu_{0,1}$[e] (mHz)	17.68 ± 0.77	10.28 ± 0.24	40.40 ± 2.93	38.81 ± 2.01	18.67 ± 2.20	19.43 ± 0.90
$\Delta\nu_1$[e] (mHz)	15.48 ± 2.05	1.28 ± 0.97	28.06 ± 11.96	18.75 ± 8.98	21.98 ± 6.23	7.08 ± 3.60
$N_{\rm QPO,2}$[e]	...	1.91 ± 0.35	...	...	...	...
$\nu_{0,2}$[e] (mHz)	...	15.05 ± 1.68	...	...	...	...
$\Delta\nu_1$[e] (mHz)	...	11.10 ± 3.05	...	...	...	...
χ^2/dof	309.83/208	753.75/764	178.14/137	128.05/97	327.11/329	268.86/267
(continuum[f])	(618.71/211)	(868.30/770)	(257.33/140)	(207.54/100)	(669.58/332)	(543.03/270)

Notes. Here, we use an energy band in which the QPO is detected with very high confidence.

[a] The good time intervals were broken into smaller intervals to improve the signal-to-noise in the power density spectra (PDS). For a given observation, the size of each segment × number of such segments is shown.

[b] The power spectrum was derived using all the photons in this energy range. For a given observation, this is an energy range in which the QPO was detected with a high significance.

[c] The count rate in the bandpass shown in the second row.

[d] We fit the continuum with a bending power-law model described as follows:

$$\text{continuum} = C + \frac{A\nu^{-\Gamma_{\rm Low}}}{1+\left(\frac{\nu}{\nu_{\rm bend}}\right)^{\Gamma_{\rm High}-\Gamma_{\rm Low}}},$$

where, $\Gamma_{\rm Low}$ and $\Gamma_{\rm High}$ are the low and high frequency slopes, respectively, and $\nu_{\rm bend}$ is the bend frequency.

[e] We model the QPOs with a Lorentzian. The functional form is as follows:

$$\text{QPO} = \frac{N_{\rm QPO}}{1+\left(\frac{2(\nu-\nu_0)}{\Delta\nu_0}\right)^2},$$

where ν_0 is the centroid frequency and $\Delta\nu_0$ is the FWHM of the QPO feature.

[f] The χ^2/dof for the continuum are shown in braces.

is evident from the best-fit parameters of the QPOs (Tables 2 and 3). More specifically, since we have smeared out the possible close pair QPOs (as reported by S07 and S09 using the 2006 and the 2008 data sets, respectively) the average quality factors of the QPOs reported here are relatively lower than those typical of the type-C QPOs from StBHs. Moreover, variation of the QPO centroid frequency over the timescale of the observation can further decrease its coherence. Furthermore, we analyzed the PDSs of the backgrounds from each of the six observations and note that they are all consistent with a constant Poisson noise.

One of the main goals of the present work is to better characterize the mHz QPOs seen from NGC 5408 X-1 within the context of the known classes of LFQPO seen in StBHs (Casella et al. 2005). An important diagnostic for this purpose is the study of the variation of the rms amplitudes of these QPOs with their centroid frequency. In the case of LFQPOs from StBH systems this behavior is fairly well established (e.g., Revnivtsev et al. 2000; Sobczak et al. 2000; Vignarca et al. 2003; McClintock & Remillard 2006). The typical behavior of the StBH LFQPOs, in the energy range 2.0–20.0 keV (the nominal *RXTE* bandpass), can be described as follows: as the source evolves along the low/hard state toward the SPL state, the QPO frequency increases and the rms amplitude increases. Before reaching the SPL state, the source traverses an "intermediate" state in which the QPO frequency continues to increase, but the rms amplitude decreases. Upon reaching the SPL state the correlation tends to break down, showing more scatter in the rms amplitude (see Figure 11 in McClintock et al. 2009).

The X-ray variability of NGC 5408 X-1 is known to depend on energy (Middleton et al. 2011). The overall rms variability increases with an increase in the energy of the photons at least up to 2.5 keV (given the poor S/N at higher energies, it is not clear whether the variability strength levels off or decreases). This is similar to the energy dependence of LFQPO (≈few Hz) detected from the galactic micro-quasar *GRS 1915+105* (Rodriguez et al. 2004), where the QPO amplitude increases with energy, before rolling over. We used the QPO fit parameters from all the observations to explore the dependence of the QPO rms amplitude with centroid frequency. To be consistent across all the observations, we chose an optimum bandpass of 1.0–10.0 keV to ensure good statistics and significant detection of the variability (the variability of the source increases at higher energies while the count rate decreases). In addition, to explore whether our results might depend on energy, we derived the QPO properties in a different energy band (though with some overlap of the optimum band defined above) of 0.5–5.0 keV. The rms amplitude versus QPO frequency results for 1.0–10.0 keV and 0.5–5.0 keV are shown in the left and right panels of Figure 3, respectively (compare with Figure 11 of McClintock et al. 2009). Given that the QPO amplitude is higher at higher energies (Middleton et al. 2011), not all power spectra derived from the lower energy band (0.5–5.0 keV) yielded statistically significant QPO features. This is why the right panel of

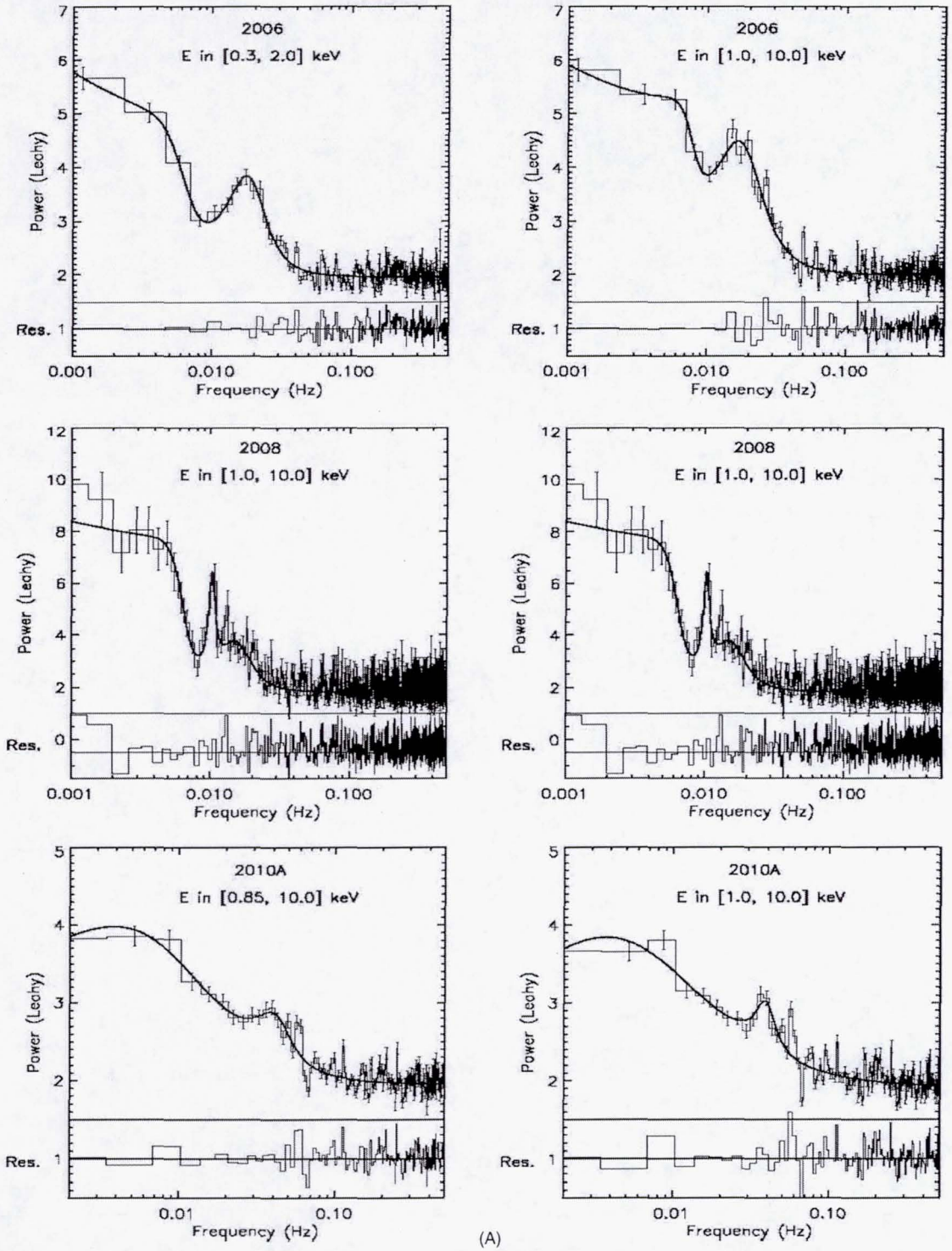

(A)

Figure 2. Power spectra derived from the first three of the six *XMM-Newton* observations ((A) 2006, 2008, and 2010A; (B) 2010B, 2011A, and 2011B; see Table 1). For a given power spectrum the strength of a QPO is dependent on the energy band under consideration. Left panel: the power spectrum using an energy band (shown at the top of each plot) in which the QPO is clearly detected. Also shown are the error bars and the residuals (data-model) offset to an arbitrary value in each case. Right panel: same as the plots on the left panel. However, here we choose a fixed energy range of 1.0–10.0 keV. A consistent energy band across all the power spectra is required to unambiguously assess the behavior (especially, rms amplitude vs. QPO centroid frequency; Figure 3) of these QPOs.

Figure 3 has one less data point. Clearly, the variation is similar in both the energy bands. We further compare with the results from StBHs in Section 5.

Another prime driver for the long observations of NGC 5408 X-1 was to search for high-frequency QPO (HFQPO) analogs of StBHs. These QPOs are observed in the range from about 50–450 Hz in StBHs (McClintock & Remillard 2006; Strohmayer 2001a). Simple mass scaling arguments would suggest that in IMBHs they would be expected in the frequency range of 0.1–1 Hz, with a low rms amplitude of ~2%. We

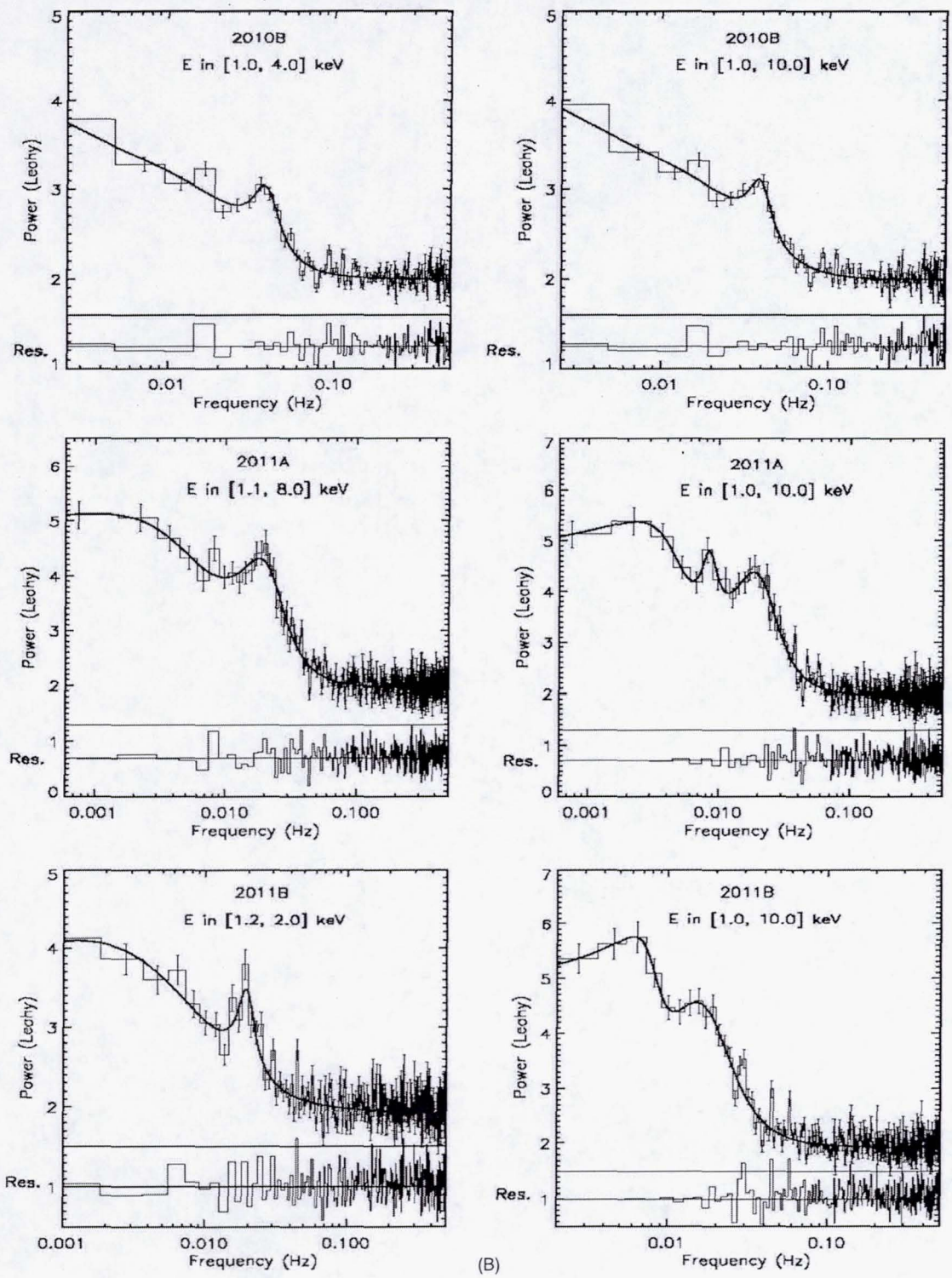

(B)

Figure 2. (Continued)

do not detect any obvious QPO-like feature at these frequencies in any of the individual observations. Further, given that HFQPOs appear to be reasonably stable in frequency in StBHs (e.g., Strohmayer 2001b), we averaged the power spectra derived from the individual observations to improve the S/N, however, this did not lead to a detection. We estimate the upper limit on the rms amplitude of a QPO-like feature in the frequency range of 0.1–1.0 Hz to be ~4%.

4. ENERGY SPECTRAL ANALYSIS

We fit the X-ray spectra of NGC 5408 X-1 using the XSPEC (Arnaud 1996) spectral fitting package and the EPIC response files were generated using the *arfgen* and *rmfgen* tools which are part of the *XMM-Newton* Science Analysis System (SAS) software. Since a primary goal of the present work is to search for timing–spectral correlations similar to those seen

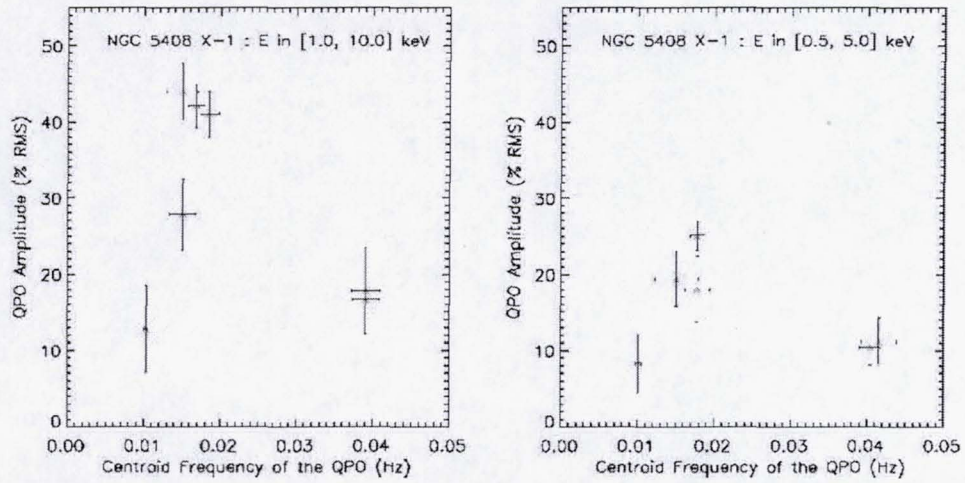

Figure 3. rms amplitude of the mHz QPOs detected from NGC 5408 X-1 (*Y*-axis) is plotted against the QPO centroid frequency (*X*-axis). To study the dependence of this plot on the bandpass, we consider two different energy bands. Left panel: centroid frequency vs. QPO amplitude using photons in the energy range from 1.0 to 10.0 keV. Right panel: same as the left panel, but a different band pass of 0.5–5.0 keV was used. The qualitative nature of the behavior does not change with the energy band under consideration. However, the rms amplitude of a given QPO seems to increase with increasing energy (at least in the two energy bands considered), i.e., higher rms amplitude in 1.0–10.0 keV compared to 0.5–5.0 keV.

(A color version of this figure is available in the online journal.)

Table 3
Summary of the Best-fitting Model Parameters for the Power Density Spectra
(PDS; Using Only Photons in the Energy Range of 1.0–10.0 keV) of the ULX NGC 5408 X-1

Data Set	2006	2008	2010A	2010B	2011A	2011B
Exposure[a] (ks)	27.6 × 3	15.5 × 2	23.2 × 3	21.0 × 4	67.4 × 1	55.0 × 1
Energy Range (keV)	1.0–10.0	1.0–10.0	1.0–10.0	1.0–10.0	1.0–10.0	1.0–10.0
Count rate[b] (counts s^{-1})	0.43 ± 0.01	0.43 ± 0.02	0.55 ± 0.02	0.53 ± 0.01	0.49 ± 0.02	0.49 ± 0.02
C[c]	2.00 ± 0.01	1.81 ± 0.02	1.90 ± 0.04	1.99 ± 0.01	1.94 ± 0.01	1.92 ± 0.01
A[d]	0.80 ± 0.89	3.39 ± 2.90	0.01 ± 0.01	$(1.48 \pm 3.88) \times 10^{-04}$	4.16 ± 11.49	2.96 ± 9.50
$\Gamma_{\rm Low}$[d]	0.20 ± 0.17	0.09 ± 0.13	1.12 ± 0.30	2.65 ± 1.06	-0.072 ± 0.39	-0.05 ± 0.56
$\nu_{\rm bend}$[d] (mHz)	7.89 ± 0.73	6.34 ± 0.49	7.12 ± 6.13	36.39 ± 21.26	4.96 ± 1.48	8.30 ± 1.15
$\Gamma_{\rm High}$[d]	10.02 ± 11.47	10.25 ± 5.60	-0.41 ± 0.46	0.25 ± 0.14	4.42 ± 7.78	9.87 ± 12.11
$N_{\rm QPO,1}$[e]	2.49 ± 0.18	3.51 ± 1.69	0.64 ± 0.15	0.67 ± 0.21	2.40 ± 0.19	2.64 ± 0.27
$\nu_{0,1}$[e] (mHz)	16.81 ± 1.05	10.28 ± 0.24	39.07 ± 1.70	39.07 ± 1.82	18.49 ± 1.28	15.04 ± 2.04
$\Delta\nu_1$[e] (mHz)	19.51 ± 2.16	1.28 ± 0.97	15.15 ± 6.44	16.04 ± 8.89	21.86 ± 2.60	22.83 ± 2.94
$\rm RMS_{QPO,1}$[e]	42.12 ± 2.83	12.81 ± 5.75	16.64 ± 4.05	17.84 ± 5.68	41.00 ± 3.05	43.94 ± 3.72
$N_{\rm QPO,2}$[e]	...	1.91 ± 0.35	...	...	1.31 ± 1.02	...
$\nu_{0,2}$[e] (mHz)	...	15.05 ± 1.68	...	...	8.40 ± 1.22	...
$\Delta\nu_1$[d](mHz)	...	11.10 ± 3.05	...	...	...	...
$\rm RMS_{QPO,2}$[e]	...	27.82 ± 4.64	...	...	3.09 ± 4.32	...
χ^2/dof	268.34/208	753.75/764	200.60/137	135.27/97	350.16/326	291.45/266
(continuum[f])	(755.28/211)	(868.30/770)	(242.10/140)	(190.64/100)	(851.45/332)	(677.00/269)

Notes.

[a] The good time intervals were broken into smaller intervals to improve the signal-to-noise in the power density spectra (PDS). For a given observation, the size of each segment × number of such segments is shown. Same time intervals as in Table 1 were used here.

[b] To systematically study the QPO properties, we reduced the power spectra in a consistent energy band of 1.0–10.0 keV.

[c] The count rate in the bandpass of 1.0–10.0 keV.

[d] We fit the continuum with a bending power-law model described as follows:

$$\text{continuum} = C + \frac{A\nu^{-\Gamma_{\rm Low}}}{1+\left(\frac{\nu}{\nu_{\rm bend}}\right)^{\Gamma_{\rm High}-\Gamma_{\rm Low}}},$$

where $\Gamma_{\rm Low}$ and $\Gamma_{\rm High}$ are the low- and high-frequency slopes, respectively, and $\nu_{\rm bend}$ is the bend frequency.

[e] We model the QPOs with a Lorentzian. The functional form is as follows:

$$\text{QPO} = \frac{N_{\rm QPO}}{1+\left(\frac{2(\nu-\nu_0)}{\Delta\nu_0}\right)^2}, \qquad \text{RMS}_{\rm QPO}(\text{integrated from } -\infty \text{ to } +\infty) = \frac{\pi N_{\rm QPO}\Delta\nu}{2} \times 100,$$

where ν_0 is the centroid frequency and $\Delta\nu_0$ is the FWHM of the QPO feature.

[f] The χ^2/dof for the continuum are shown in braces.

in accreting StBHs, we began our analysis by characterizing the energy spectra using the same phenomenological models often used to describe the X-ray spectra of accreting StBHs. In terms of XSPEC models, we used *diskpn + power-law*. We also explored the *bmc* model, Comptonization by bulk motion (Titarchuk et al. 1997), because it has been used to derive mass estimates from QPO frequency scaling arguments, and reference spectral–timing correlations have been derived for a significant sample of StBHs using the parameters derived from this model (see Shaposhnikov & Titarchuk 2009). We start by describing some of the specifics of our data extraction and reduction methods.

Since we are interested in exploring the correlations between the timing and the spectral behavior, we elected to extract energy spectra from the same time intervals as those used to extract the PDS (see the first row of Tables 1 and 2). Such synchronous measurements will tend to minimize any offsets that could be induced by variations in the system properties (both spectral and timing) within a given observation. In addition to the standard filters described in Section 2, the *(FLAG==0)* filter was imposed to get the highest quality spectra. The combined (*pn+MOS*) average count rate of the source varied in the range 1.19–1.46 counts s^{-1} over all the observations. Given such relatively low count rates, source pileup was not an issue in any of the six observations. Since we are using both the *pn* and the *MOS* data, we individually reduce the energy spectra from each of the detectors using the same GTIs. This gave us three energy spectra (*pn, MOS1, MOS2*) for each of the six observations. A given model was fit simultaneously to all the three spectra to derive the tightest constraints on the best-fit parameters. The *pn* and the *MOS* spectra were binned to one-third of the FWHM of the pn and the MOS spectral resolution, respectively. We used the SAS task *specgroup* for this purpose. Given the high number of total counts ($\approx$(6–12) $\times$ 10,000), this gave us high-quality spectra in each case.

We began by fitting the spectra with a multi-colored disk (*diskpn* in XSPEC; Gierliński et al. 1999) + power-law (*powerlaw* in XSPEC) + an X-ray hot plasma (*apec* in XSPEC) as in S09. We used the Tuebingen–Boulder ISM absorption model (*tbabs* in XSPEC) to account for interstellar absorption. The hydrogen column density was set as a free parameter. This model is very similar to that often used to model the spectra of StBHs. Indeed, it is common to use this or similar phenomenological models to determine the spectral state of an StBH. However, here, in addition to a thermal disk and a corona, there is an X-ray emitting plasma in the model. This was realized by S07 after identifying systematic emission-like features in the residuals of the *diskpn + power-law* fit to the 2006 data. We confirm their result that the χ^2 improves significantly (by $\sim$40–100 over all the six observations) with addition of the *apec* component to the standard *multi-colored disk + power-law* model. Such a feature is not exclusive to the ULX in NGC 5408, as NGC 7424 (Soria et al. 2006c) and Holmberg II X-1 (Dewangan et al. 2004) also show evidence for the presence of an X-ray emitting plasma. In addition, the high-resolution VLA radio observations at 4.9 GHz of the counterpart of the X-ray source in NGC 5408 X-1 revealed a radio nebula of $\approx$40 pc extent (Lang et al. 2007). Based on the value of the power-law index of the radio spectrum, it was suggested that the radio emission is likely from an optically thin synchrotron emitting gas. Given this, it is possible that the putative X-ray hot plasma is coincident with the radio nebula. The best-fitting parameters of the above model for each of the six observations are shown in the top panel of Table 4. We note that the X-ray temperature of the plasma has remained constant across the suite of our *XMM-Newton* observations.

We also fit the spectra with a model based on Componization by bulk motion (Laurent & Titarchuk 1999; *bmc* in XSPEC). As mentioned above, this model has been used within the context of quantifying timing–spectral correlations in StBHs (Shaposhnikov & Titarchuk 2009). The underlying physical basis of this model is similar to that of the multi-colored disk + power-law model, i.e., the presence of a thermal disk and a hot electron corona. However, in this case the power law is produced by the Comptonization of soft photons (from the disk) within a converging inflow onto the black hole. In this model, the normalization parameter derived from the fit mimics the disk flux from the *diskpn* component in the other model we have employed. We also include the *apec* component in this case. The best-fitting model parameters including the absorbing hydrogen column density using the *tbabs* in XSPEC for each of the six data sets are shown in the bottom panel of Table 4.

It can be noted straightaway that, for a given observation, the plasma temperatures (*apec*) found from fitting the two spectral models are consistent with each other (within the error bars). The reduced χ^2 values for the *diskpn+powlaw+apec* and the *bmc+apec* model are in the range of 1.0–1.6 and 1.0–1.3 ($\sim$210–290 degrees of freedom; last column of Table 4), respectively. Clearly, they both give acceptable values of reduced χ^2. The latter model (*bmc+apec*) fits the data slightly better (see Table 4) than the simple *diskpn+apec+powlaw* model. However, the improvement in χ^2 is not statistically significant in all the cases and therefore it is not possible to rule out one model over the other based on the reduced χ^2 alone. A sample energy spectrum (using the 2010B data) is shown in Figure 4. Also shown in the figure are the ratios of the data to the folded model in the two cases (*diskpn+apec+powlaw* and *bmc+apec*). We use the spectral parameters derived here and the timing properties from the previous section to search for correlations between the two. The results of which are presented in the next section.

It has been recently suggested (Gladstone et al. 2009) that the high-quality X-ray spectra of ULXs can be better characterized by complex Comptonization models that predict a rollover at higher energies ($\gtrsim$3 keV). A detailed study of the validity of such models in the case of NGC 5408 X-1 is beyond the scope of the present work; however, for the sake of completeness we also fit all our energy spectra with a cutoff power-law component rather than just the simple power-law model. In XSPEC we used the model, *tbabs*(diskpn+apec+cutoffpl)* (the *cutoffpl* model describes a power law with a high-energy exponential rollover.) The best-fitting parameters for this model are shown in Table 5. We note that this model leads to a significant improvement in the χ^2 compared to the *tbabs*(diskpn+apec+pow)* model (compare the last column of Table 5 with the last column of Table 4). We also searched for possible timing–spectral correlations within the context of the *cutoff power-law* model, viz., QPO frequency versus the cutoff energy. We do not detect any clear correlation between the QPO frequency and the rollover energy. This is mainly due to poor statistics at the high end ($\gtrsim$5 keV) of the energy spectra which result in large uncertainties on the rollover energies.

The measurement of fluorescent lines from elements such as Fe, Ni, Cr, Ca, etc., is another important probe of the vicinity of the X-ray emitting region. In principle, these reflection features can be produced by hard X-rays, presumably from the Comptonizing corona, irradiating cold material, e.g., in the disk. Among all such emission lines with their rest-frame energies in

Table 4
Summary of the Energy Spectral Modeling of NGC 5408 X-1

tbabs(diskpn+apec+pow)*							
Data Set	n_H^a	T_{max}^b	kT_{plasma}^c	Γ^d	$Flux^e_{0.3-10.0\,keV}$	$Flux^f_{Disk}$	χ^2/dof
2006	$14.21^{+0.87}_{-0.84}$	$0.141^{+0.005}_{-0.005}$	$1.00^{+0.04}_{-0.04}$	$2.66^{+0.04}_{-0.04}$	$4.03^{+0.17}_{-0.39} \times 10^{-12}$	$1.74^{+0.14}_{-0.28} \times 10^{-12}$	431.07/265
2008	$14.67^{+1.61}_{-1.48}$	$0.136^{+0.010}_{-0.009}$	$0.95^{+0.06}_{-0.06}$	$2.59^{+0.06}_{-0.06}$	$3.83^{+0.24}_{-0.68} \times 10^{-12}$	$1.56^{+0.24}_{-0.66} \times 10^{-12}$	227.40/210
2010A	$14.41^{+1.01}_{-0.96}$	$0.144^{+0.007}_{-0.006}$	$1.01^{+0.04}_{-0.04}$	$2.58^{+0.04}_{-0.04}$	$4.55^{+0.22}_{-0.43} \times 10^{-12}$	$1.72^{+0.08}_{-0.35} \times 10^{-12}$	403.69/277
2010B	$13.04^{+0.84}_{-0.80}$	$0.154^{+0.007}_{-0.007}$	$0.99^{+0.05}_{-0.05}$	$2.58^{+0.04}_{-0.04}$	$4.05^{+0.15}_{-0.33} \times 10^{-12}$	$1.33^{+0.11}_{-0.25} \times 10^{-12}$	429.91/288
2011A	$14.58^{+0.94}_{-0.90}$	$0.146^{+0.007}_{-0.006}$	$0.95^{+0.06}_{-0.07}$	$2.63^{+0.04}_{-0.04}$	$4.22^{+0.19}_{-0.37} \times 10^{-12}$	$1.59^{+0.17}_{-0.33} \times 10^{-12}$	430.67/267
2011B	$13.44^{+1.04}_{-0.99}$	$0.154^{+0.009}_{-0.008}$	$1.01^{+0.07}_{-0.07}$	$2.55^{+0.05}_{-0.05}$	$3.84^{+0.16}_{-0.38} \times 10^{-12}$	$1.41^{+0.15}_{-0.36} \times 10^{-12}$	326.50/256
tabs(bmc+apec)*							
Data Set	n_H	kT^g_{disk}	$\alpha = \Gamma^h - 1$	f^i	N^j_{BMC}	kT^c_{plasma}	χ^2/dof
2006	$9.47^{+1.04}_{-1.00}$	$0.116^{+0.004}_{-0.004}$	$1.68^{+0.04}_{-0.04}$	$0.40^{+0.05}_{-0.05}$	$3.12^{+0.31}_{-0.27} \times 10^{-5}$	$1.03^{+0.04}_{-0.04}$	342.95/265
2008	$10.79^{+1.89}_{-1.78}$	$0.110^{+0.007}_{-0.006}$	$1.59^{+0.06}_{-0.06}$	$0.39^{+0.10}_{-0.10}$	$3.10^{+0.63}_{-0.47} \times 10^{-5}$	$0.97^{+0.05}_{-0.05}$	210.30/210
2010A	$9.73^{+1.26}_{-1.22}$	$0.116^{+0.005}_{-0.005}$	$1.59^{+0.04}_{-0.04}$	$0.45^{+0.08}_{-0.08}$	$3.35^{+0.40}_{-0.33} \times 10^{-5}$	$1.03^{+0.04}_{-0.04}$	359.92/277
2010B	$7.90^{+1.09}_{-1.05}$	$0.121^{+0.005}_{-0.005}$	$1.60^{+0.03}_{-0.03}$	$0.52^{+0.09}_{-0.08}$	$2.75^{+0.26}_{-0.22} \times 10^{-5}$	$1.03^{+0.05}_{-0.04}$	364.36/288
2011A	$9.61^{+1.16}_{-1.11}$	$0.118^{+0.005}_{-0.005}$	$1.64^{+0.04}_{-0.04}$	$0.46^{+0.07}_{-0.07}$	$3.07^{+0.33}_{-0.28} \times 10^{-5}$	$0.99^{+0.05}_{-0.05}$	361.46/267
2011B	$8.69^{+1.32}_{-1.25}$	$0.121^{+0.006}_{-0.006}$	$1.57^{+0.04}_{-0.04}$	$0.47^{+0.08}_{-0.08}$	$2.74^{+0.33}_{-0.26} \times 10^{-5}$	$1.05^{+0.09}_{-0.06}$	299.37/256

Notes. Top panel: best-fitting parameters for the *tbabs*(diskpn+apec+pow)* model. Bottom panel: Best-fitting parameters for the *tbabs*(bmc+apec)* model.

[a] Total column density of hydrogen along the line of sight including the Galactic extinction (in units of 10^{20} cm^{-2}). We used the *tbabs* model in XSPEC.

[b] Accretion disk temperature in keV. We used the *diskpn* model in XSPEC. The inner radius of the disk was fixed at $6GM/c^2$.

[c] The temperature of the surrounding plasma in keV. We used the *apec* model in XSPEC. The abundances were fixed at the solar value.

[d] The photon index of the power law.

[e] The total unabsorbed X-ray flux (in units of erg cm^{-2} s^{-1}) in the energy range of 0.3–10.0 keV.

[f] The disk contribution to the total X-ray flux (in units of erg cm^{-2} s^{-1}) in the energy range of 0.3–10.0 keV.

[g] The color temperature of the disk blackbody spectrum (in keV).

[h] Spectral index of the power-law portion of the energy spectrum.

[i] The Comptonized fraction: fraction of the input blackbody photons that are Comptonized by the bulk motion of the in-falling material.

[j] The normalization of the disk blackbody spectrum (in units of $(L/10^{39}$ erg s$^{-1})/(d/10$ kpc$)^2$). This is an indicator of the disk flux.

Table 5
Summary of the Energy Spectral Modeling of NGC 5408 X-1

tbabs(diskpn+apec+cutoffpl)*						
Data Set	n_H^a	T_{max}^b	kT_{plasma}^c	Γ^d	$E^e_{roll\ over}$	χ^2/dof
2006	$12.03^{+0.97}_{-0.94}$	$0.153^{+0.006}_{-0.006}$	$1.03^{+0.05}_{-0.04}$	$1.88^{+0.20}_{-0.21}$	$3.80^{+1.23}_{-0.79}$	375.48/264
2008	$12.93^{+1.78}_{-1.66}$	$0.146^{+0.011}_{-0.010}$	$0.97^{+0.06}_{-0.06}$	$1.92^{+0.33}_{-0.37}$	$4.29^{+3.96}_{-1.51}$	214.02/209
2010A	$11.96^{+1.15}_{-1.10}$	$0.160^{+0.008}_{-0.008}$	$1.04^{+0.05}_{-0.05}$	$1.84^{+0.20}_{-0.22}$	$4.18^{+1.52}_{-0.93}$	357.17/276
2010B	$10.53^{+1.03}_{-0.99}$	$0.171^{+0.009}_{-0.008}$	$1.02^{+0.06}_{-0.06}$	$1.92^{+0.18}_{-0.20}$	$4.92^{+1.83}_{-1.11}$	385.27/287
2011A	$12.30^{+1.09}_{-1.05}$	$0.160^{+0.008}_{-0.008}$	$0.98^{+0.06}_{-0.07}$	$1.92^{+0.21}_{-0.23}$	$4.28^{+1.70}_{-1.01}$	389.94/266
2011B	$11.54^{+1.24}_{-1.18}$	$0.167^{+0.010}_{-0.009}$	$1.05^{+0.10}_{-0.08}$	$1.98^{+0.24}_{-0.26}$	$5.56^{+3.72}_{-1.69}$	307.22/255

Notes. Best-fitting parameters for the *tbabs*(diskpn+apec+cutoffpl)* model are shown.

[a] Total column density of hydrogen along the line of sight including the Galactic extinction (in units of 10^{20} cm^{-2}). We used the *tbabs* model in XSPEC.

[b] Accretion disk temperature in keV. We used the *diskpn* model in XSPEC. The inner radius of the disk was fixed at $6GM/c^2$.

[c] The temperature of the surrounding plasma in keV. We used the *apec* model in XSPEC. The abundances were fixed at the solar value.

[d] The photon index of the cutoff power law.

[e] The energy at which the exponential rollover of the spectrum occurs.

the *XMM-Newton* bandpass (0.2–10.0 keV), the iron feature is the most prominent (e.g., Matt et al. 1997). Given the subtle changes in the energy spectra over the suite of observations (see Table 4), it does not seem unreasonable to combine all the data while searching for weak emission features. We searched for iron emission line features in the energy range of 6.0–7.0 keV, but did not detect any obvious features. Using an effective exposure of ≈540 ks (all data sets; see Table 1), we were able to place tight constraints on the equivalent width of any feature in the energy range of 6.0–7.0 keV. Assuming an unresolved narrow feature of width 10 eV, the upper limit (90% confidence) on the equivalent width of an emission line at 6.4 keV is 5.4 eV. We then check for the possibility of broad emission lines in the energy range 6.0–7.0 keV. The upper limits on the equivalent width assuming a broad emission line of width 0.3 keV and 1.0 keV are 11.6 eV and 11.0 eV, respectively.

The apparent weakness of iron emission from the disk can be due to a number of factors: an accretion disk that is completely ionized, scattering of the reflected iron-line photons in an optically thick corona (Matt et al. 1997), especially when the

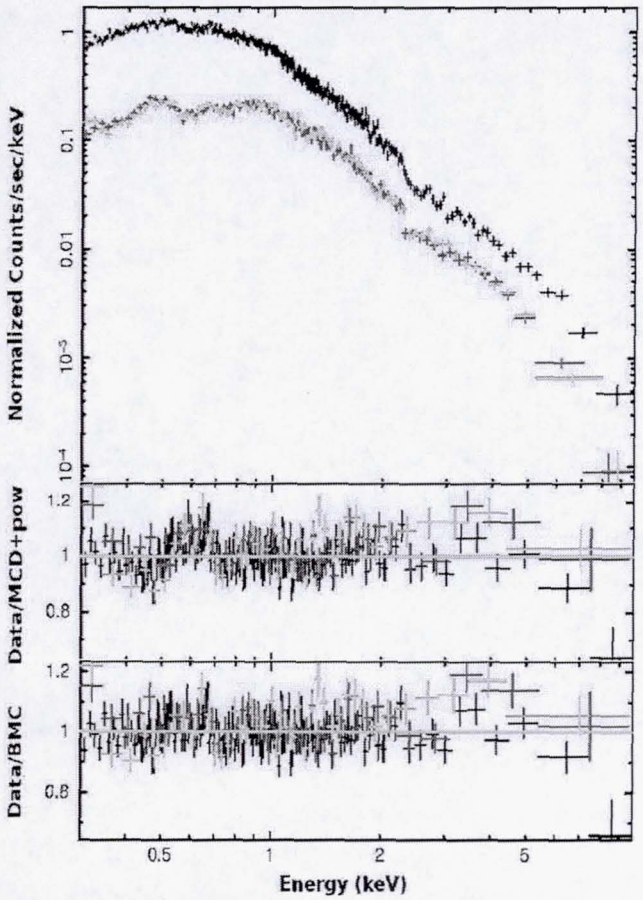

Figure 4. Top panel: the X-ray energy spectrum (0.3–10.0 keV) of NGC 5408 X-1 derived from the *2010B* observation (Table 1). The data from all the three detectors are shown. Black corresponds to EPIC-pn, while green and red represent data from the MOS1 and MOS2 detectors, respectively. The spectrum was re-binned for clarity to have a significant detection of at least 10σ. However, no more than 10 neighboring bins were combined to achieve this level of significance, i.e., *setplot rebin 10 10* in XSPEC. Middle panel: the ratio of the data to the model defined by *tbabs*(diskpn + apec + powerlaw)* is shown. Bottom panel: the ratio of the data to the model defined by *tabs*(bmc+apec)* is shown. Both the ratios were re-binned to have a detection significance of at least 20 with no more than 20 neighboring bins combined, i.e., *setplot rebin 20 20* in XSPEC.

(A color version of this figure is available in the online journal.)

corona is a thin layer above the accretion disk or a low iron abundance in the accretion disk (Matt et al. 1997). Further, a high inclination angle for the accretion disk combined with one or more of the above factors can decrease the intensity of the iron line. Recently, Gladstone et al. (2009) have analyzed energy spectra of a sample of ULXs (including NGC 5408 X-1) and have suggested that these sources might be operating in a new accretion state, with rollover at higher energies (>2.0 keV) as a characteristic signature of such a state. Thus, the nature of the spectrum might be such that there are not enough photons at higher energies to generate a detectable iron-line fluorescent feature (M. C. Miller 2011, private communication).

5. TIMING–SPECTRAL CORRELATIONS

A primary goal of the new observations of NGC 5408 X-1 is to further test the preliminary classification of the mHz QPOs detected from NGC 5408 X-1 as the analogs of the 0.1–15 Hz low-frequency, type-C QPOs (LFQPOs) detected from accreting StBHs. If a strong connection can be demonstrated, then scaling of the characteristic frequencies (e.g., QPO centroid frequency) can be better justified to estimate the mass of the black hole within this source.

As mentioned earlier, scaling relations using the PDS break frequency have been successfully tested using power spectra of both stellar and SMBHs of known mass (McHardy et al. 2006; Körding et al. 2007). Based on the qualitative nature of the PDS and the energy spectra derived using the 2006 and 2008 data, S09 suggested that the mHz QPOs from NGC 5408 X-1 may indeed be LFQPO analogs. More specifically, they proposed that its X-ray state was analogous to that of an StBH in the so-called SPL state exhibiting type-C QPOs, but at the same time emitting a few $\times 10$ higher X-ray flux. Having analyzed the data from all six observations (Sections 3 and 4) we confirm that the derived power- and energy-spectral parameters are qualitatively consistent with the source being in an SPL state exhibiting type-C QPOs (based on the state descriptions in McClintock & Remillard 2006). A summary of the working definition of the SPL state with type-C QPOs and the PDS and energy spectral parameters of NGC 5408 X-1 are given in Table 6.

A further step in understanding the nature of these QPOs is to determine if they show the same evolutionary behavior in the QPO parameters as those exhibited by the StBH LFQPOs. One such characteristic behavior is the QPO rms amplitude versus centroid frequency relationship. Our results for this relation from NGC 5408 X-1 are shown in the left and right panels of Figure 3 in two different energy bands (1.0–10.0 keV and 0.5–5.0 keV, respectively). Comparing these plots with those from StBHs, as in Figure 11 of McClintock et al. (2009), the results appear to be at least qualitatively consistent with the behavior of SPL data from some StBHs (see, for example, the green triangles in Figure 11 of McClintock et al. 2009). However, because a tight correlation appears to break down in the SPL state it is hard to conclude definitively that the NGC 5408 X-1 behavior is exactly analogous.

Another important signature of the Type-C LFQPOs in StBHs is their dependence on the energy spectral features, i.e., the timing–spectral correlations. Using the X-ray state classifications as in McClintock & Remillard (2006), LFQPOs in StBHs are usually detected in the low/hard state, SPL state, and during the transition between these two states. Within the context of the multi-colored disk + power-law model parameters, it is known that the centroid frequency of these LFQPOs is correlated with the disk flux and the photon index of the power-law component. In StBHs, the typical behavior is that the QPO centroid frequency is positively correlated with the disk flux and the photon index of the power law. At a certain higher QPO centroid frequency ($\approx$5–10 Hz) the relationship seems to flatten (saturate) and even appears to start reversing in some cases (Vignarca et al. 2003). Furthermore, the correlation is not exactly the same for all StBHs, i.e., the value of the slope of the correlation and the photon index/disk flux at saturation are different for different sources and can be different for the same source in a different outburst (Vignarca et al. 2003; Shaposhnikov & Titarchuk 2009). In Figure 5, we show plots of several derived spectral parameters and fluxes (using the *diskpn + power-law* fits) as a function of the QPO centroid frequency. These can be compared with similar plots derived from StBH systems (see, for example, Figures 8 and 9 in McClintock et al. 2009; Figure 10 of Vignarca et al. 2003). Again, there appears to be qualitative consistency between the behavior exhibited by NGC 5408 X-1 and StBHs, but the full

Table 6
Comparing the PDS and the Energy Spectral Properties of NGC 5408 X-1 with the Steep Power-law (SPL) State in Stellar-mass Black Holes

X-Ray State	Definition[a]
Steep Power-law State (SPL)	Presence of power-law component with $\Gamma > 2.4$ Power continuum: $r^b < 0.15$ Either disk fraction[c] <80% and 0.1–30 Hz QPOs present with rms amplitude >0.01 or disk fraction[c] <50% with no QPOs present
X-Ray State	**Data from NGC 5408 X-1[d]**
Steep Power-law State ? (SPL)	Presence of power-law component with Γ in the range 2.5–2.7 Power continuum: r^e in the range ≈0.36–0.43 Disk fraction[f] in the range ~30%–50% and 10–40 mHz QPOs present with rms amplitude in the range 0.10–0.45

Notes.
[a] In case of stellar-mass black holes, the definition is using data in the energy range of 2–20 keV.
[b] Total rms power integrated over 0.1–10.0 Hz.
[c] Fraction of the total 2–20 keV unabsorbed flux.
[d] In case of NGC 5408 X-1, we use the *XMM-Newton* bandpass of 0.3–10.0 keV.
[e] We integrate the total power (continuum + QPOs) in the frequency range of 0.001–0.5 Hz (same as the frequency range used for power spectra fitting). The power spectra were derived using all the photons in the energy range of 1.0–10.0 keV (see Table 3 for the parameters).
[f] Fraction of the total 0.3–10 keV unabsorbed flux.

range of behavior is not yet seen, again because the range of spectral variations in NGC 5408 X-1 (most notably in the power-law index) is too modest. Additional measurements of QPO properties at lower values of the power-law photon index, for example, could provide a more definitive test.

One can also investigate the spectral–temporal correlations in the context of the spectral parameters derived using the *bmc* model. Indeed, Shaposhnikov & Titarchuk (2009) explored such correlations in detail for a sample of StBHs using *RXTE* data. They also developed a set of fitting functions to quantify the observed correlations and used these to obtain mass estimates by scaling arguments. Figure 5(B) compares the results from NGC 5408 X-1 with those from StBHs using the *bmc* spectral fits. We used the published data from Shaposhnikov & Titarchuk (2009) to produce representative plots for an StBH (XTE J1550−564, top panels). Shown from left to right are the QPO centroid frequency versus the power-law photon index (Γ), the *bmc* normalization (disk flux) versus Γ and the Comptonized fraction, f versus Γ, respectively. The data points are color coded to highlight the low/hard state (blue) and the SPL state (green). We used the data from the 1998 outburst of XTE J1550−564 which clearly demonstrates the typical behavior of StBHs (top panels). Comparisons of these plots with those in, for example, Shaposhnikov & Titarchuk (2009) lead to similar conclusions as with the results in Figure 5(A). There is qualitative consistency with the Type-C identification, but the classification is not definitive. In order to make a more secure association of the QPOs in NGC 5408 X-1 with Type-C (SPL state) QPOs in the StBHs, we need, at a minimum, to obtain observations of the source over a greater range of power-law spectral indices.

6. DISCUSSION

It has been established that black hole masses scale with the break frequency of their PDS (McHardy et al. 2006; Körding et al. 2007) and this relation is known to hold over six orders of magnitude in mass, i.e., from StBH to SMBHs. Furthermore, at least in StBHs, the break frequency of the PDS is known to strongly correlate with the centroid frequency of the LFQPOs (Wijnands & van der Klis 1999). Therefore, it is reasonable to assume that the mass of the black hole scales with the centroid frequency of the LFQPOs. This can be especially useful in cases where black hole mass measurements are otherwise difficult, viz., in ULXs. However, an important caveat is to ensure that the QPOs used for comparison are similar in nature.

Our new results confirm the earlier result from S09 that the qualitative nature of the PDS and the energy spectrum of NGC 5408 X-1 are very similar to that of StBHs in the SPL state (see Table 6). At the same time, the characteristic timescales within the PDS are lower by a factor of ≈100, while the X-ray luminosity is higher by a factor of a few ×10, when compared to a typical StBH in such a state. However, based on the scaling between the break frequency of the PDS and the centroid frequency of the LFQPOs (centroid frequency of LFQPOs ≈ 12 × break frequency of the PDS), the association of the mHz QPOs from NGC 5408 X-1 with the LFQPOs from StBHs has been questioned (Middleton et al. 2011).

A striking feature of the behavior of NGC 5408 X-1 is that the energy spectrum of the source has remained roughly constant over the current suite of observations, while the properties of the most prominent QPO (e.g., rms amplitude, centroid frequency) have changed significantly. These results appear consistent with the source being in a spectral state similar to the SPL state in StBHs. More specifically, in StBHs, certain spectral properties like the disk flux, the photon index of the power law correlates positively with the QPO centroid frequency up to a certain frequency (≈2–10 Hz) beyond which the relationship turns around or remains roughly constant. Detailed analysis of the timing–spectral correlations in StBH sources such as XTE J1550−564 and H1743−322 has revealed a comprehensive picture (McClintock et al. 2009) of their behavior. Tracking these two sources as they evolved from the low/hard state into the SPL state, it was realized that the spectral properties like the disk flux and the power-law photon index are tightly correlated with the QPO centroid frequency during the low/hard state and during a transition phase intermediate between the low/hard and the SPL state; and the relationships seem to saturate/breakdown (spectral properties remain roughly constant with increase in the

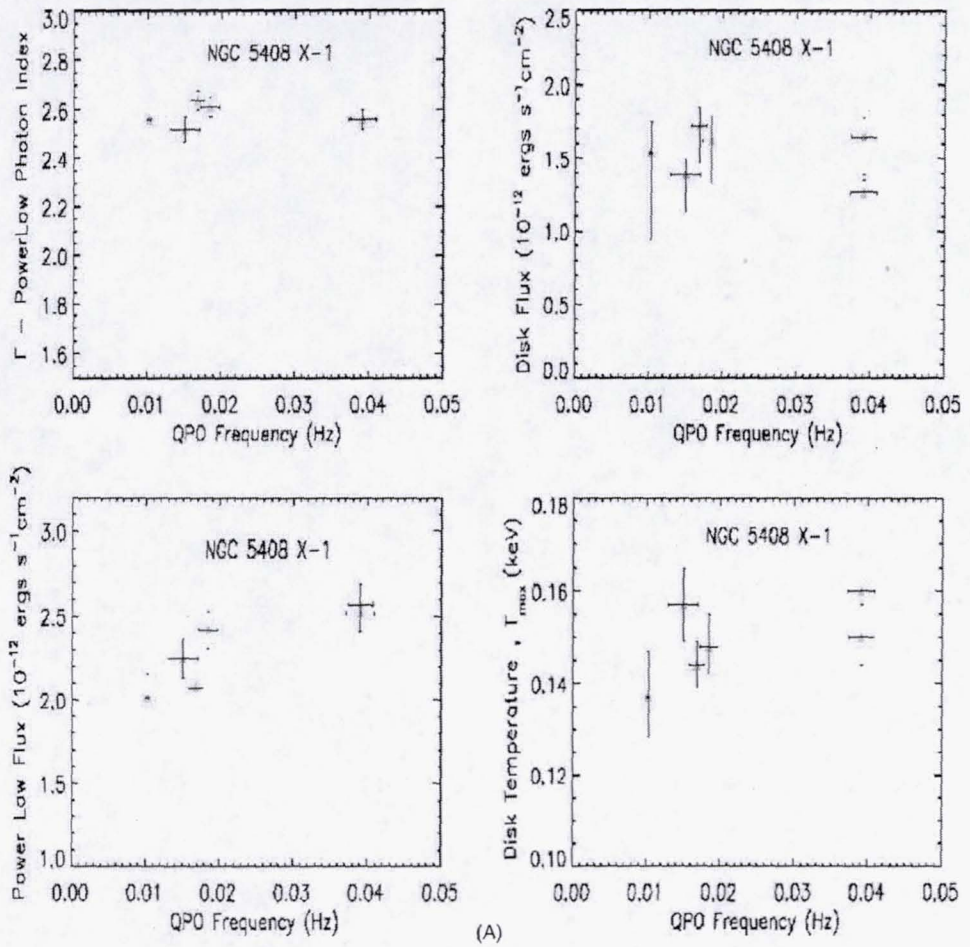

Figure 5. (A) Timing–spectral correlations using the phenomenological model: diskpn + powerlaw. Six observations/data points were used to search for timing–spectral correlations. Top left panel: the photon index of the power law (*Y*-axis) is plotted against the centroid frequency of the QPO (*X*-axis). Top right panel: the disk contribution to the total flux (*Y*-axis) in the energy range of 0.3–10.0 keV is plotted against the centroid frequency of the QPO. Bottom left panel: flux from the power-law component (*Y*-axis) is plotted against the QPO centroid frequency (*X*-axis). Bottom right panel: for the sake of completeness, the disk temperature (*Y*-axis) is plotted against the QPO centroid frequency (*X*-axis). Within the present scheme of X-ray states in StBHs, these results are qualitatively consistent with NGC 5408 X-1 being in the steep power-law state exhibiting type-C QPOs, with the characteristic timescales scaled down by a factor of ≈a few ×10. (B) Timing–spectral correlations using the BMC model. Top panels: the behavior of a typical stellar-mass black hole (1998 outburst of StBH XTE J1550−564) is shown (we plot data from Shaposhnikov & Titarchuk 2009). For clarity, the X-ray state of the source is highlighted using the following color scheme. Blue squares indicate the low/hard state, magenta corresponds to a state intermediate between the low/hard and the SPL state, while the green triangles highlight the SPL state. From left to right, the dependence of the centroid frequency of the QPO, BMC normalization (disk flux), and the comptonized fraction on the power-law index are shown. The error bars are not indicated when their size is smaller than the size of the data point. Bottom panel: similar plots using the data from NGC 5408 X-1. The results from the ULX NGC 5408 X-1 are qualitatively consistent with the source being in an X-ray state very similar to the steep power-law state in stellar-mass black holes (compare with the green triangles on the top panel).

(A color version of this figure is available in the online journal.)

QPO frequency) as the sources entered the SPL state. It may be that we are in fact seeing NGC 5408 X-1 in a similar state, that is, we may be seeing the "saturated" portion of the relation.

Given that the overall accretion timescales change with the mass of the black hole (timescales increase as the mass increases from StBHs to SMBHs, e.g., McHardy et al. 2006), it is possible that we are seeing a similar timing–spectral behavior, and that the apparent longevity of the source in the SPL state might also be due to its having a higher mass. There may be a useful analogy to AGNs in that their spectra are known to remain roughly constant on timescales of at least a few years (Markowitz et al. 2003), while transient StBH systems undergo strong energy spectral changes on timescales of the order of a few days (McClintock & Remillard 2006 and references therein). It could be that the persistence of NGC 5408 X-1 in the approximately same spectral state is related to it being of intermediate mass between StBHs and AGNs. Alternatively, perhaps the source is in an accretion state, like the so-called ultraluminous state of Gladstone et al. (2009), that is just not well sampled by the behavior of Galactic StBHs. We note that the indication for a rollover in the power law at 4–5 keV (see Section 4 and Table 5) provides some support for this interpretation, in which case the spectral state of NGC 5408 X-1 may not be exactly analogous to the SPL state of StBHs.

However, either conclusion will remain tentative until NGC 5408 X-1 is observed in a state with a lower value of the power-law photon index, i.e., a state similar to the low/hard state in StBHs. Such an observation would clearly be important in order to make a more definitive identification of its QPOs in the context of those observed in StBHs.

Assuming the constancy of the energy spectral features, i.e., disk flux, Γ, with the increasing QPO centroid frequency (see Figure 5) is analogous to the saturation observed in the timing–spectral correlations in StBHs, one can estimate the

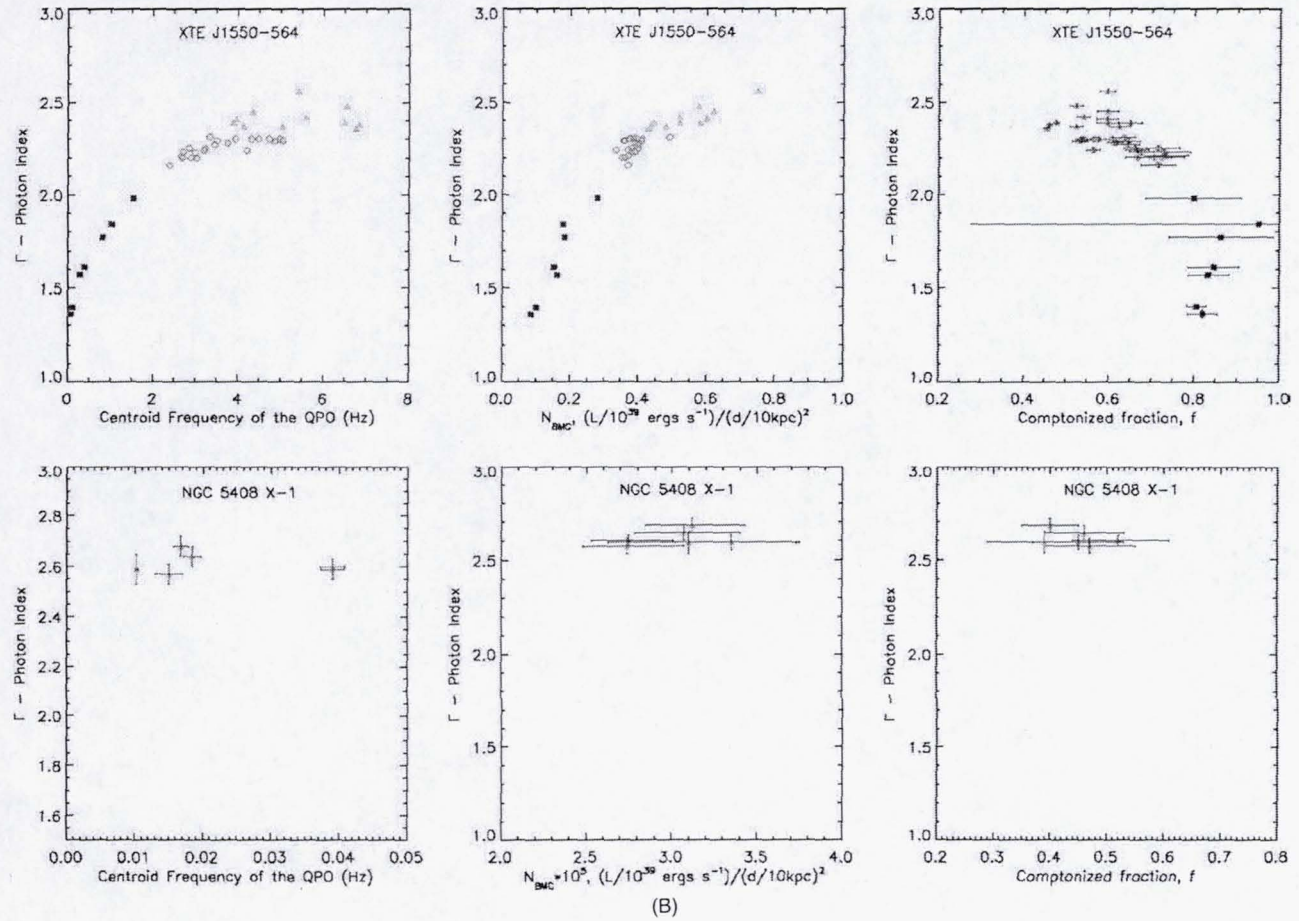

Figure 5. (Continued)

minimum mass of the black hole in NGC 5408 X-1. If we are indeed seeing only the saturated portion of the complete timing–spectral correlation curve, then the minimum QPO frequency observed in NGC 5408 X-1 serves as an upper limit on the so-called transition frequency, i.e., the frequency beyond which the timing–spectral correlations tend to saturate. In order to derive a mass estimate, this particular frequency can be scaled to a reference StBH of known mass with a measured transition frequency ($\nu_{\rm trans}$). We can use the transition frequency as defined by Shaposhnikov & Titarchuk (2009) in their fits of QPO and spectral parameters. We find a sample of three StBHs with mass and transition frequency measurements in Shaposhnikov & Titarchuk (2009) that are suitable for this purpose. Further, it is known that the same source can exhibit different tracks (timing–spectral correlation curves), i.e., different transition frequencies, in various outburst episodes. Given that we are interested in a lower limit on the mass of the black hole in NGC 5408 X-1, we consider the lowest transition frequency for a given source. The minimum mass of the black hole in NGC 5408 X-1 can then be calculated as $\nu_{\rm trans} \times {\rm Mass}_{\rm Reference}/({\rm minimum\ QPO\ frequency})$. The mass estimates using the three reference sources, GRO 1655−40, XTE J1550−564, and GX 339−4, are reported in Table 7 ($\sim$1000 $M_{\odot}$) and show substantial overlap with those reported by S09.

Table 7
Mass Estimate of the Black Hole in NGC 5408 X-1

Reference	Mass ($M_{\odot}$)	$\nu_{\rm trans}$[a] (Hz)	Min. Mass$^{\rm b}_{\rm NGC\ 5408}$ ($M_{\odot}$)	References
GRO J1655−40	6.3 ± 0.5	3.0 ± 0.1	1720	1, 4
XTE J1550−564	9.5 ± 1.1	1.84 ± 0.07	1490	2, 4
GX 339−4	>6	1.4 ± 0.2	820	3, 4

Notes.
[a] The transition frequencies were estimated by Shaposhnikov & Titarchuk (2009). The fitting functions for the timing–spectral correlations are described therein.
[b] Minimum mass of the black hole in the ULX $= (\nu_{\rm trans} \times {\rm mass})_{\rm ReferenceStBH}/10.28$ mHz, where 10.28 mHz is the minimum QPO frequency detected from NGC 5408 X-1. We consider the error bars on the individual parameters and report the lower value of the mass.
References. (1) Greene et al. 2001; (2) Orosz et al. 2002; (3) Muñoz-Darias et al. 2008; (4) Shaposhnikov & Titarchuk 2009.

7. SUMMARY

The ULX in the irregular dwarf galaxy, NGC 5408 has been suggested to harbor an intermediate-mass black hole (${\rm Mass_{BH}} \approx 100$ to a few $\times$ 1000 $M_{\odot}$) (S09). This mass estimate was strictly based on the assumption that the mHz QPOs seen from this source are the type-C analogs of the low-frequency QPOs (0.1–15 Hz) from StBHs. Here we have presented results from new observations of NGC 5408 X-1 in which we searched for timing–spectral correlations similar to those often exhibited by the type-C LFQPOs from StBHs. Our analysis of multi-epoch *XMM-Newton* data from NGC 5408 X-1 reveals that certain characteristic features of the power spectra, especially the QPO centroid frequency, changed significantly. However,

the energy spectrum has remained roughly constant. These results can be interpreted in two ways. This could be due to complete independence of the timing properties on the energy spectra, unlike StBHs, in which case mass scalings derived from the QPOs are likely to be problematic; or there is in fact a correlation, but we are seeing only the saturated part of the correlation behavior (constancy of the Γ/disk flux with increasing QPO frequency). Such saturation is often seen in StBHs (e.g., Vignarca et al. 2003). Assuming we are seeing this saturated portion of the correlation curve, we estimate the lower limit on the mass to be $\approx 800\ M_{\odot}$. At least one observation with the source in a low/hard-like state ($\Gamma < 2.0$) is necessary to resolve the issue of whether the timing and spectral properties are correlated as in StBHs or not.

REFERENCES

Arnaud, K. A. 1996, in ASP Conf. Ser. 101, ed. G. H. Jacoby & J. Barnes (Astronomical Data Analysis Software and Systems V; San Francisco, CA: ASP), 101, 17
Begelman, M. C. 2002, ApJ, 568, L97
Begelman, M. C., Volonteri, M., & Rees, M. J. 2006, MNRAS, 370, 289
Belloni, T., Psaltis, D., & van der Klis, M. 2002, ApJ, 572, 392
Casella, P., Belloni, T., & Stella, L. 2005, ApJ, 629, 403
Colbert, E. J. M., & Mushotzky, R. F. 1999, ApJ, 519, 89
Davies, M. B., Miller, M. C., & Bellovary, J. M. 2011, ApJ, 740, L42
Dewangan, G. C., Miyaji, T., Griffiths, R. E., & Lehmann, I. 2004, ApJ, 608, L57
Dewangan, G. C., Titarchuk, L., & Griffiths, R. E. 2006, ApJ, 637, L21
Fabbiano, G. 1989, ARA&A, 27, 87
Farrell, S. A., Webb, N. A., Barret, D., Godet, O., & Rodrigues, J. M. 2009, Nature, 460, 73
Feng, H., Rao, F., & Kaaret, P. 2010, ApJ, 710, L137
Gierliński, M., Zdziarski, A. A., Poutanen, J., et al. 1999, MNRAS, 309, 496
Gladstone, J. C., Roberts, T. P., & Done, C. 2009, MNRAS, 397, 1836
Greene, J., Bailyn, C. D., & Orosz, J. A. 2001, ApJ, 554, 1290
Immler, S., & Lewin, W. H. G. 2003, in Supernovae and Gamma-Ray Bursters, ed. K. Weiler (Berlin: Springer-Verlag), 91
Kaaret, P., Prestwich, A. H., Zezas, A., et al. 2001, MNRAS, 321, L29
King, A. R., Davies, M. B., Ward, M. J., Fabbiano, G., & Elvis, M. 2001, ApJ, 552, L109
Körding, E. G., Migliari, S., Fender, R., et al. 2007, MNRAS, 380, 301
Körding, E., Falcke, H., & Markoff, S. 2002, A&A, 382, L13
Lang, C. C., Kaaret, P., Corbel, S., & Mercer, A. 2007, ApJ, 666, 79
Laurent, P., & Titarchuk, L. 1999, ApJ, 511, 289
Leahy, D. A., Darbro, W., Elsner, R. F., et al. 1983, ApJ, 266, 160
Mack, K. J., Ostriker, J. P., & Ricotti, M. 2007, ApJ, 665, 1277
Markowitz, A., Edelson, R., & Vaughan, S. 2003, ApJ, 598, 935
Matsumoto, H., Tsuru, T. G., Koyama, K., et al. 2001, ApJ, 547, L25
Matt, G., Fabian, A. C., & Reynolds, C. S. 1997, MNRAS, 289, 175
McClintock, J. E., & Remillard, R. A. 2006, in Compact Stellar X-ray Sources, ed. W. Lewin & M. van der Klis (Cambridge: Cambridge Univ. Press), 157
McClintock, J. E., Remillard, R. A., Rupen, M. P., et al. 2009, ApJ, 698, 1398
McHardy, I. M., Koerding, E., Knigge, C., Uttley, P., & Fender, R. P. 2006, Nature, 444, 730
Middleton, M. J., Roberts, T. P., Done, C., & Jackson, F. E. 2011, MNRAS, 411, 644
Miller, M. C., & Colbert, E. J. M. 2004, Int. J. Mod. Phys. D, 13, 1
Miller, M. C., & Hamilton, D. P. 2002, MNRAS, 330, 232
Miniutti, G., Ponti, G., Dadina, M., et al. 2006, MNRAS, 373, L1
Muñoz-Darias, T., Casares, J., & Martínez-Pais, I. G. 2008, MNRAS, 385, 2205
Orosz, J. A., Groot, P. J., van der Klis, M., et al. 2002, ApJ, 568, 845
Rao, F., Feng, H., & Kaaret, P. 2010, ApJ, 722, 620
Revnivtsev, M. G., Trudolyubov, S. P., & Borozdin, K. N. 2000, MNRAS, 312, 151
Rodriguez, J., Corbel, S., Hannikainen, D. C., et al. 2004, ApJ, 615, 416
Shaposhnikov, N., & Titarchuk, L. 2009, ApJ, 699, 453
Sobczak, G. J., McClintock, J. E., Remillard, R. A., et al. 2000, ApJ, 531, 537
Soria, R., Kuncic, Z., Broderick, J. W., & Ryder, S. D. 2006, MNRAS, 370, 1666
Strohmayer, T. E. 2001a, ApJ, 552, L49
Strohmayer, T. E. 2001b, ApJ, 554, L169
Strohmayer, T. E., & Mushotzky, R. F. 2003, ApJ, 586, L61
Strohmayer, T. E., & Mushotzky, R. F. 2009, ApJ, 703, 1386
Strohmayer, T. E., Mushotzky, R. F., Winter, L., et al. 2007, ApJ, 660, 580
Titarchuk, L., Mastichiadis, A., & Kylafis, N. D. 1997, ApJ, 487, 834
van der Klis, M. 1989, in Timing Neutron Stars, ed. H. Ogelmann (NATO ASI, Series C; Dordrecht: Reidel), 27
Vignarca, F., Migliari, S., Belloni, T., Psaltis, D., & van der Klis, M. 2003, A&A, 397, 729
Volonteri, M., Haardt, F., & Madau, P. 2003, ApJ, 582, 559
Wijnands, R., & van der Klis, M. 1999, ApJ, 514, 939